RESEARCH ARTICLE

Correspondence to:
E. D. Johnson,
ejohnson@whoi.edu

Remote determination of the velocity index and mean streamwise velocity profiles

E. D. Johnson[1,2] and **E. A. Cowen[1]**

[1]DeFrees Hydraulics Laboratory, School of Civil and Environmental Engineering, Cornell University, Ithaca, New York, USA
[2]Applied Ocean Physics and Engineering, Woods Hole Oceanographic Institution, Woods Hole, Massachusetts, USA

Abstract When determining volumetric discharge from surface measurements of currents in a river or open channel, the velocity index is typically used to convert surface velocities to depth-averaged velocities. The velocity index is given by, $k = U_b/U_{surf}$, where U_b is the depth-averaged velocity and U_{surf} is the local surface velocity. The USGS (United States Geological Survey) standard value for this coefficient, $k = 0.85$, was determined from a series of laboratory experiments and has been widely used in the field and in laboratory measurements of volumetric discharge despite evidence that the velocity index is site-specific. Numerous studies have documented that the velocity index varies with Reynolds number, flow depth, and relative bed roughness and with the presence of secondary flows. A remote method of determining depth-averaged velocity and hence the velocity index is developed here. The technique leverages the findings of Johnson and Cowen (2017) and permits remote determination of the velocity power-law exponent thereby, enabling remote prediction of the vertical structure of the mean streamwise velocity, the depth-averaged velocity, and the velocity index.

1. Introduction

When quantifying volumetric discharge from free-surface velocity measurements, the velocity index, $k = U_b/U_{surf}$, which is equal to the ratio of the depth-averaged velocity to the surface velocity, is typically used to convert free-surface velocities to depth-averaged velocities. The seminal work of *Rantz* [1982] first established the velocity index coefficient from a series of experiments (conducted by *Hulsing et al.* [1966]) and it was found that a value of $k = 0.85$ for natural channels and $k = 0.90$ for concrete-lined channels resulted in errors of less than $\pm 5\%$ in the determination of volumetric discharge. This default value assumes mean streamwise velocity profiles follow the standard logarithmic-law distribution. Since this seminal work, it has become standard practice within the hydraulic community to apply the value $k = 0.85$ to free-surface velocity measurements in the determination of volumetric discharge. This is particularly true for field measurements [e.g., *Muste et al.*, 2004; *Puleo*, 2012; *Costa et al.*, 2000; *Creutin*, 2003; *Melcher et al.*, 2002; *Kim et al.*, 2008; *Tsubaki et al.*, 2011; *Hauet et al.*, 2008].

However, recent experiments have demonstrated that the precise value of the velocity index is a function of Reynolds number, location of measurement, and bed roughness condition. It can also be influenced by changes in the river stage and by the presence of secondary currents, vegetation, and tidal fluctuations. It is not surprising that the velocity index is a function of Reynolds number. Yet there have been relatively few studies that systematically investigate this effect. *Johnson and Cowen* [2016] systematically varied the Reynolds number ($Re_h = U_b h/\nu$, where h is the flow depth and ν is the kinematic viscosity) from 4950 to 73,800 in their laboratory experiments over a smooth bed and found that the velocity index varied from $k = 0.82$ to 0.93. The observed variation was strongly correlated with the ratio of the displacement thickness (equation (2)) to flow depth ($R^2 = 0.96$), illustrating that subtle changes in the mean streamwise velocity profile resulting from changes in Reynolds number, influence depth-averaged velocity and, in turn, the velocity index. The field measurements of *Harpold et al.* [2006] also observed Reynolds number variation and used a value of 0.85 for base flow conditions and 0.93 at high-flow conditions.

Variations in the river cross section can also lead to variation in the velocity index. As *Rantz* [1982] and *Muste et al.* [2008] point out, the precise value of the velocity index is unique to a particular channel and location of measurement in the channel cross section. *Rantz* [1982] demonstrates that the values of the velocity
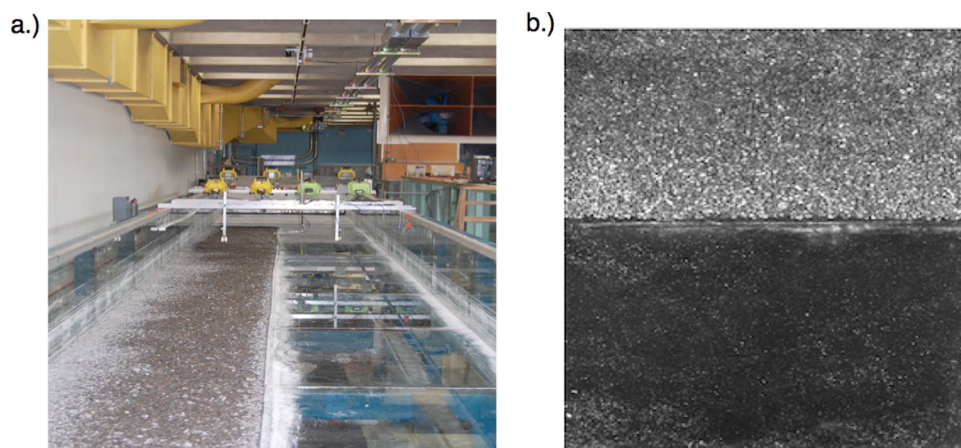
Figure 1. (a) Rough bed experimental setup. (b) Rough bed camera field-of-view [*Johnson and Cowen*, 2016].

index increases in the vicinity of the channel wall [*Rantz*, 1982, Figure 89]. *Muste et al*. [2011] further suggest that for flows in natural rivers the velocity index could vary widely over the river cross section [see *Muste et al*., 2011, Figure 7d] and that the application of a singular constant may be inappropriate.

The influence of secondary currents on the velocity index has been demonstrated by *Gunawan et al*. [2012] who measured lateral variations of k, which ranged from $k = 0.86$ to 1.18. They demonstrate that the velocity index is highly dependent on the structure of the flow and, when the dominant flow becomes three-dimensional, it becomes possible for the velocity index to exceed unity, $k > 1$ [*Gunawan et al*., 2012, Figure 1]. Similarly, *Sun et al*. [2010], in their study of discharge estimation in a small river, found that in situations in which the flow is highly three-dimensional, such as in compound or irregular channels, the velocity index varies considerably from the USGS standard value. They found the velocity index ranged from approximately $k = 0.79$ to 1.72 for inbank and overbank conditions.

A number of studies have also documented the effect that variable bed roughness conditions can have on the velocity index. In a series of laboratory experiments involving a smooth bed, a rough bed (k-type roughness), and a bed with stationary dunes *Polatel* [2006] found that the velocity index ranged from 0.79 to 0.93. *Johnson and Cowen* [2016] in their study of smooth and gravel beds found that the velocity index varied from 0.69 to 0.94. *Le Coz et al*. [2010] also note the site-specific nature of the velocity index and for typical values of relative roughness they calculate values of the velocity index of $k = 0.79$ to 0.89 based on a logarithmic profile.

Considering specific bed types, *Le Coz et al*. [2010] found that a coefficient of $k = 0.90$ best fit their measurements made in a river with a bed composed of limestone bedrock. *Dramais et al*. [2011] obtained the range, $k = 0.72$ to 0.79 in the gravel-bed rivers in which they conducted their measurements. During high-flow conditions in a mountain stream, *Jodeau et al*. [2008] determined that the range $k = 0.75$ to 0.83, best described their data.

The work of *Gunawan et al*. [2012] also considered the influence that submerged vegetation can have on the lateral variation of the velocity index. The canopy flow they observed as a result of the vegetation resulted in a decrease in the velocity index to $k = 0.397$. The influence of the submerged vegetation substantially decreased the depth-averaged velocity yet had a smaller effect on the surface velocity. This resulted in a dramatic decrease in the velocity index.

Complexities present in tidally influenced rivers and canals, which include flow reversals, salinity intrusions, and changes in water level, often create conditions in which the velocity index varies widely from the USGS standard velocity-index. *Rantz* [1982] anticipated variation in the velocity index with river stage, citing the change in the vertical distribution of velocity as the cause. Variation in the velocity index with stage can also be deduced in the results of *Johnson and Cowen* [2016], who systematically varied the flow depth while maintaining constant values of depth-averaged velocity (see their Figure 5 and Tables 1–3).

Table 1. Smooth Bed Cases and Power-Law Fits

h (m)	U_B (m/s)	Re_h^a	Fr^b	u^* (mm/s)^c	m	R^2
0.06	0.23	14,606	0.33	14.0	5.57	0.91
0.06	0.35	21,795	0.46	18.0	9.43	0.84
0.10	0.05	4,948	0.05	3.0	6.66	0.93
0.10	0.09	9,574	0.10	6.1	6.24	0.99
0.10	0.23	23,396	0.25	11.8	9.84	0.96
0.10	0.33	32,895	0.36	18.0	7.63	0.99
0.15	0.05	7,023	0.04	2.8	7.23	0.95
0.15	0.10	14.543	0.08	6.0	7.71	0.94
0.15	0.24	35,835	0.20	12.0	9.03	0.97
0.15	0.34	50,935	0.29	16.0	9.12	0.98
0.20	0.05	10,654	0.04	3.0	7.88	0.95
0.20	0.10	19,649	0.07	5.2	9.07	0.93
0.20	0.24	48,704	0.18	12.0	12.75	0.93
0.20	0.34	70,033	0.26	16.5	12.40	0.93
0.30	0.10	29,095	0.06	5.5	13.09	0.85
0.30	0.24	73,747	0.14	11.0	14.83	0.90

[a]Re_h is the Reynolds number formed with the depth-averaged velocity and flow depth.
[b]Fr is the Froude number formed with the centerline velocity and flow depth.
[c]u^* is the friction velocity.

Rantz [1982] also notes that in tidally influenced streams, where flow reversal frequently occurs, the velocity index may vary with the tidal cycle. To illustrate this variation, *Rantz* [1982] cites the field experiments of *Smith* [1969] during which the velocity index varied with the tidal cycle between $k = 0.96$ to 1.04. To address these complexities, determination of the variation of the velocity index as a function of stage and tidal cycle were recommended. *Bechle et al.* [2012] observed similar variations in their experiments in a wide tidal estuary, where during low tide the balance of a baroclinic density current and a barotropic pressure difference resulted in mean velocity profiles that varied drastically from the standard log-law profile [*Bechle et al.*, 2012, Figure 11], resulting in a velocity index, $k = 1.26$ to 1.63. During slack tide they observed a two-layer structure in the mean velocity profile and the corresponding velocity index was $k = 0.30$. During ebb tide, the velocity profiles where much more consistent with the log law; hence, values for the velocity index were closer to the USGS standard, $k = 0.90$ to 0.92.

It can be concluded from these investigations that the velocity index is a site-specific parameter that can vary locally as conditions change. It is a function of Reynolds number, flow depth, channel aspect ratio, bed roughness type, and relative roughness (h/z_o, where h is the flow depth and z_o is the roughness length), and local bathymetric and vegetative conditions. Given the complexity inherent in the riverine environment, the application of a singular laboratory-derived coefficient leads to inadequate characterization of the vertical flow structure over a given channel cross section and inaccurate estimates of volumetric discharge.

Dramais et al. [2011], in their assessment of dominant sources of error in their Large-scale Particle Image Velocimetry (LSPIV) technique, found that the multiplicative error induced by the velocity index was a major source of error. While other sources of error (including uncertainty in water level, free-surface deformations resulting from waves, total number of image pairs, insufficient tracer particles, and orthorectification errors) resulted in total error between 1–5%, they estimated errors resulting from velocity coefficient variability to be 10–15%. As *Le Coz et al.* [2010] point out, the velocity index causes multiplicative and systematic error of

Table 2. Rough Bed Cases and Power-Law Fits

h (m)	U_B (m/s)	Re_h	Fr	u^* (mm/s)	k_{rms}/h	m	R^2
0.06	0.05	4,893	0.11	17.0	0.29	2.76	0.97
0.01	0.05	6,018	0.08	8.2	0.20	2.94	0.99
0.15	0.06	10,430	0.08	5.4	0.14	3.50	0.98
0.20	0.04	7,735	0.04	3.4	0.11	4.21	0.97
0.20	0.08	13,674	0.06	8.0	0.11	3.89	0.98
0.20	0.18	36,804	0.16	17.5	0.10	3.82	0.99
0.20	0.22	51,671	0.24	19.0	0.11	3.76	0.99

Table 3. Asymmetric Compound Channel Cases and Power-Law Fits

h (m)	y/B	U_B (m/s)	u^* (mm/s)	Fr	m	R^2
0.15	−0.35	0.22	11.5	0.19	7.73	0.97
0.15	−0.08	0.21	17.0	0.24	6.09	0.93
0.20	−0.35	0.23	10.5	0.19	9.80	0.94
0.20	−0.08	0.23	13.0	0.21	6.23	0.97
0.20	0.08	0.20	15.0	0.20	5.46	0.98
0.26	−0.08	0.24	12.0	0.19	8.18	0.92
0.26	0.08	0.22	12.0	0.19	6.94	0.98
0.26	0.35	0.18	14.0	0.22	5.69	0.99

LSPIV discharge estimates, it is therefore imperative that a methodology be developed that allows remote determination of this coefficient.

Here we develop a remote method of ascertaining the vertical structure of the streamwise velocity and the velocity index over a channel cross section. The technique developed leverages the findings of *Johnson and Cowen* [2017] and approaches the problem of remotely predicting the vertical structure of the streamwise velocity using a power-law representation. In the following section, a brief description of the experimental methods used in this study are described. A more thorough treatment of the experimental methods can be found in *Johnson* [2015], *Johnson and Cowen* [2016], and *Johnson and Cowen* [2017]. Section 3 outlines our approach for the remote prediction of the vertical structure of the streamwise velocity and velocity index. This is followed by the conclusion section in which implications for field application are discussed.

2. Experimental Methods

A series of Large-scale Particle Image Velocimetry (LSPIV) and Acoustic Doppler Velocimetry (ADV) measurements were conducted in a recirculating, wide-open channel flume, which is 15 m long, 2 m wide, and 0.64 m deep. The channel and experimental protocol are described in detail in *Johnson and Cowen* [2016] and *Johnson* [2015]. All the measurements reported herein were made ∼9 m downstream from the beginning of the test section, allowing sufficient distance for the boundary layer to develop fully. The mean streamwise velocity fields measured by the LSPIV system showed little variation ($<10\%$) in the streamwise direction over the camera's field-of-view, verifying that the flow had indeed achieved a fully developed state. The coordinate system used in these experiments has its origin at the beginning of the test section, along the channel centerline, at the channel bed. The x, y, and z coordinates designate the streamwise, transverse and vertical directions, respectively.

2.1. Experimental Cases

Twenty-six experimental flow cases were completed and are summarized in Tables (1–3). Sixteen cases were conducted in which the channel's smooth glass walls comprised the flow boundary conditions. In the smooth bed cases, the flow depth ranged from $h = 0.06$ to 0.31 m and the flow speed was systematically varied such that depth-averaged velocity ranged from $U_B = 0.05$ to 0.34 m/s (Table 1) [*Johnson and Cowen*, 2016].

Seven cases were conducted in which a bed of loose gravel (median and rms particle size $D_{50} = 6$ mm, $k_{rms} = 21.6$ mm, respectively) was added to half of the channel. The gravel was added in a strip that was 12 m long and ∼0.90 m wide (spanning $0.05 \leq y/B \leq 0.5$, where B is the channel width equal to 2 m, see Figure 1). It ran from the beginning of the test section to well past the location where the measurements were made, allowing sufficient distance for the resulting flow to develop fully. The gravel was leveled by hand before the experiments were run and no motion of the bed material was observed during the experiments. This was confirmed through visual assessment of the LSPIV images. For the rough bed cases, the flow depth varied from $h = 0.08$ to 0.21 m and the depth-averaged velocity ranged from $U_B = 0.4$ to 0.22 m/s (Table 2) [*Johnson and Cowen*, 2016].

Three experimental cases were completed for which a PVC false-bottom section was added to the channel (Figure 2) to create an asymmetric compound channel. The maximum height of the added PVC section is 0.16 m. The height of the section decreases linearly over an 0.80 m span, creating bathymetry that varies in the lateral direction. Two experiments were conducted where the channel was filled above the maximum
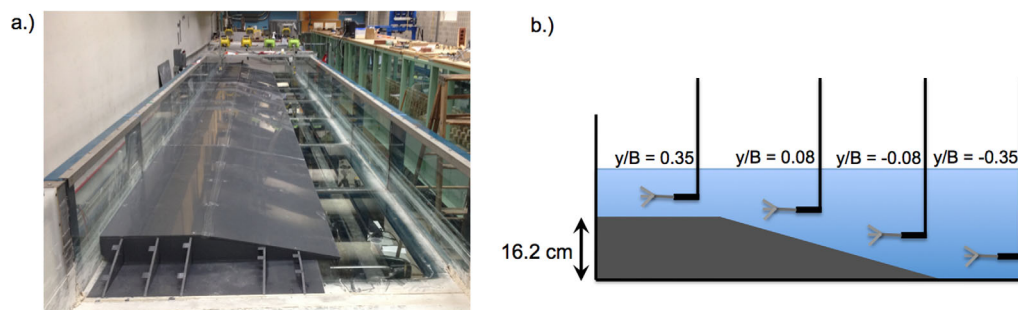
Figure 2. (a) Compound channel experimental setup. Note: Front cover of the false-bottom inset has been removed to reveal the cross section. (b) Compound channel schematic with ADV measurement positions indicated [*Johnson and Cowen*, 2016].

height of the added PVC section ($h = 0.20$ and 0.26 m), creating overbank flow conditions and a flood plain. One experiment was conducted at bank-full conditions ($h = 0.15$ cm) [*Johnson and Cowen*, 2016].

2.2. Large-Scale Particle Image Velocimetry (LSPIV) Experiments

To quantify the free-surface velocity field, LSPIV measurements were conducted for each experimental case listed in Tables 1–3. The method used here involves capturing a rapid series of images of the free surface of an open channel flow that has been seeded with small buoyant particles. The average displacement of a small cloud of tracer particles is the same as the average displacement of that region of surface fluid and when divided by the elapse time between images, yields an instantaneous surface velocity vector [e.g., *Cowen and Monismith*, 1997; *Willert and Gharib*, 1991]. The instantaneous velocity fields captured in successive images can be averaged in time to determine the mean velocity field [*Johnson and Cowen*, 2016].

A brief overview of the experimental setup is described here; details on the experimental setup and image analysis can be found in *Johnson and Cowen* [2016] and *Johnson* [2015]. The field-of-view (FOV) of the IMPERX BobCat GEV camera used in these experiments is approximately 2.03×1.93 m. The images span the entire width of the channel in the spanwise direction ($y = \pm1.00$) and $x = 8.87$ to 10.9 m in the streamwise direction. The spatial resolution of the camera, which is a function of flow depth, ranged from 1.01 to 1.08 mm/pixel. A total of at least 4000 image pairs (the elapse time between image pairs was $\Delta t = 0.75$ to 400 ms) were captured at a sampling frequency of 1 Hz for each data set. A constant light source was provided through eight 500 W halogen lamps (four on the upstream side of the FOV and four on the downstream side). The particles that are imaged in these experiments are Pliolite VTAC-L particles manufactured by OMNOVA. The particle sized ranged from 0.42 to 0.6 mm and the Stokes number for the particles is $St = \tau U_o/d_C = 0.024$ (where τ is the characteristic particle time, U_o is the typical flow speed, and d_C is the characteristic eddy diameter), indicating that the particles have ample time to adjust to the fluid flow and are well-characterized as passive tracers. All of the images were preprocessed using a stationary background subtraction developed by *Mejia-Alvarez and Christensen* [2013] and *Honkanen and Nobach* [2005] and then subsequently analyzed using an improved version of the cross-correlation algorithm described in *Cowen and Monismith* [1997]. The subwindow size used by the cross-correlation algorithm was set at 64×32 pixels (approximately 0.06×0.03 m in the streamwise and transverse directions, respectively).

2.3. Acoustic Doppler Velocimetry Measurements

To characterize the vertical structure of the streamwise velocity, vertical profiles of the three-component velocity were measured for each experimental case using a Nortek Vectrino ADV (equipped with +firmware). Five minutes of data were acquired at each vertical position at a sample rate of 200 Hz. The signal-to-noise ratio of these measurements was on average 16 dB and the correlation values were high (>93%) [*Johnson and Cowen*, 2016]. For the smooth glass bed experiments, profiles were measured at the channel centerline ($y/B = 0$). For the gravel bed cases, measurements over the center of the gravel strip ($y/B = 0.23$) are reported here. For the compound channel cases, profiles were measured in the center of the main channel ($y/B = -0.35$), and when the flow depth permitted, measurements were made in two locations over the variable bathymetry between the main channel and flood plain ($y/B = \pm0.08$) and in one location over the floodplain ($y/B = 0.35$) (Figure 2b).

2.4. Measurement Uncertainty

The bias and random error present in the measurements reported herein were quantified for each experimental case and the worst-case error for all experiments is reported here. Bias errors are deterministic and result from a systematic deviation present in the measurement system. They can generally be accounted for if the source is known. Random error can arise from multiple sources. They generally have a mean equal to zero and a nonzero variance. The random error was quantified for each experimental case using the bootstrap method [*Efron and Tibshirani*, 1993]. For this technique, the data are resampled 1000 times with replacement and the statistic of interest is calculated from each replicate set. The 90% uncertainty interval is determined from the ordered bootstrap generated, where the 50th and 950th order values are taken as the 5% and 95% statistic.

For all of the experimental cases, the worst-case bias error for the free-surface velocity measurements resulting from calibration errors was ± 7 mm/s and the worst-case random error was ± 3 mm/s. For the ADV measurements, the worst-case bias error is ± 0.3 mm/s (results from uncertainty in the probes vertical position) and the worst-case random error is ± 0.3 mm/s.

The largest source of error in our measurements stems from estimating the friction velocity. The friction velocity is an inherently challenging parameter to measure and is known to be prone to higher uncertainty. As will be discussed in section 3.2, we used seven different methods to estimate the friction velocity and found that the estimates agreed within 30%. While this level of agreement is consistent with the results of *Bagherimiyab and Lemmin* [2013] and *Nezu and Nakagawa* [1993] among others, it does introduce error in our results.

3. Results

3.1. Power-Law Representation of the Streamwise Velocity Profiles

In developing a strategy to remotely determine depth-averaged velocity, we first establish that our data are well approximated by an empirical power-law velocity distribution. The representation of the vertical distribution of streamwise velocity by a power law has a long history in communities concerned with wall-bounded flows, i.e., the open channel, riverine, turbulent and atmospheric boundary layer, urban canopy, and pipe flow communities. In particular, the velocity power law has a long history in the flow resistance research community. It is well known that the logarithmic law can be approximated by a power law in the overlap and outer layer portions of the boundary layer [see *Hinze*, 1959, Figure 7–2]. Indeed, *Cheng* [2007] in a study of open channel flows demonstrates that the power law is a first-order approximation of the log-law [see *Cheng*, 2007, Figure 2].

The applicability of both laws has been discussed and debated in the literature. *Chen* [1991] and *Schlichting* [1960] note that the log law should be regarded as an asymptotic law, which is applicable to high Reynolds numbers, whereas the power law is valid even at lower Reynolds numbers. The logarithmic law is theoretically applicable in the near-bed overlap region only (the lower 20–30% of the flow depth) [*Cheng*, 2007; *Pope*, 2000; *Nezu and Nakagawa*, 1993; *Lee et al.*, 2013], whereas the power law has been found to apply to a larger fraction of the water column. *Ligrani* [1989] notes that the power-law distribution reasonably represents the outer layer and portions of the log-law region and further states that the representation is poor in the viscous sublayer.

The power-law form of the vertical velocity distribution, assuming the form given by *Cheng* [2007], is,

$$\frac{U(z)}{U_{\max}} = \left(\frac{z}{h}\right)^{1/m}, \tag{1}$$

where $U(z)$ is the mean streamwise velocity as a function of vertical position, $1/m$ is the power-law exponent, and h represents the flow depth. For open channel flow, U_{max}, which is the maximum streamwise velocity, is taken to be the velocity at the free surface, i.e., $U_{max} = U_{surf}$ [*Cheng*, 2007; *Nowell and Church*, 1979]. Alternate formulations of the power law, where the local streamwise velocity, $U(z)$, is normalized by the friction velocity include a multiplicative constant on the right-hand side which has been demonstrated to be a function of the Reynolds number [*Chen*, 1991].
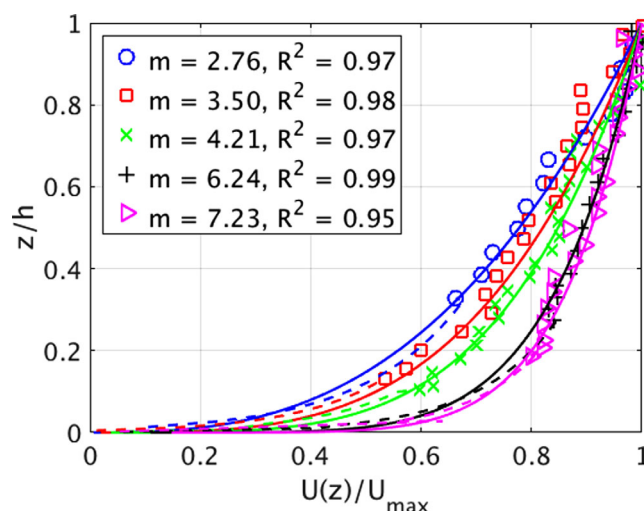
Figure 3. Typical mean streamwise velocity power-law curve fits from the smooth bed and rough bed and asymmetric compound channel cases. Discrete data points are ADV measurements. Dotted line is the log law. Solid line is the power law.

As for the power-law exponent, Prandtl first suggested that the 1/7th ($m = 7$) power law is applicable to turbulent boundary layers. Many other early flow resistance researchers followed, suggesting coefficients in the range, $m = 4$ to 12 [*Lacey*, 1946; *Manning*, 1891, 1895; *Blasius*, 1913; *Williams and Hazen*, 1933]. Since these early studies, the power-law exponent has been demonstrated to be a function of Reynolds number and relative bed roughness. Coefficients in the range of $m = 4$ to 12 [*Chen*, 1991] (for fully rough and hydraulically smooth bed conditions) and $m = 2$ to 6 [*Smart*, 2002] (for gravel beds with high relative roughness) have been found applicable to a broad range of env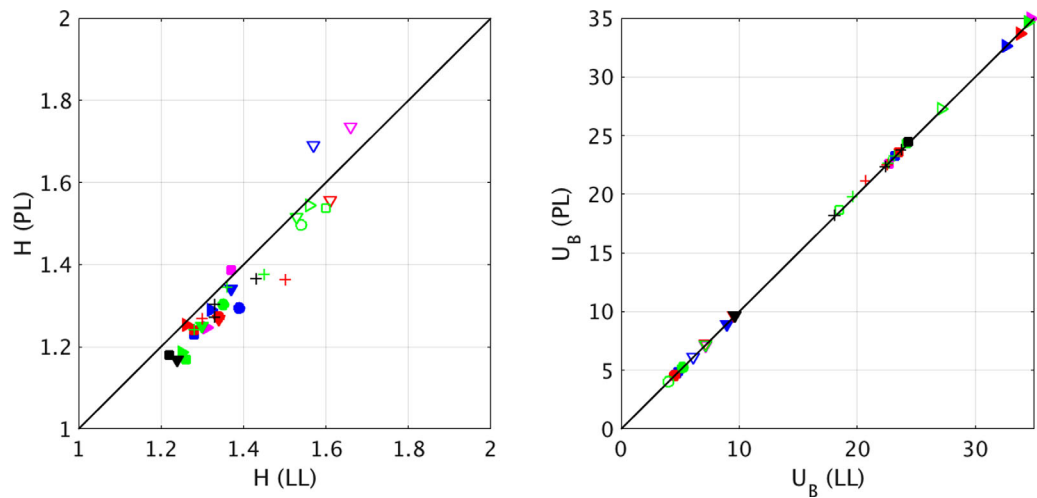ironmental and laboratory flows. Given this spread in experimentally measured exponents, *Chen* [1991] concluded that particular values of m are applicable for a limited range of Reynolds numbers.

All of the experimental flow cases reported herein were fit to the power-law profile given by equation (1), where the near surface (i.e., $z/h > 0.95$) velocity measured by the ADV was used to normalize the profiles. Tables 1–3 include the results from curve fits for each experimental case along with the R^2 value, which relates the goodness-of-fit. Note that each curve fit was performed by omitting the top most data point of each profile which was often affected by the ADV protruding through the water surface (ADV was position laterally in the flow). Values of the power-law coefficient range from $m = 5.6$ to 14.8, $m = 2.8$ to 4.2, $m = 5.5$ to 9.8 for the smooth bed, rough bed, and compound channel flow cases, respectively. In general, the data are well approximated by the power law, and for the majority of the experimental cases, R^2 exceeds 0.90. The exceptions are the shallowest cases ($h \approx 0.06$ m) for which it was difficult to accurately measure a 0.06 m water column with a 0.03 m ADV probe. It can also be observed that the deeper cases ($h \geq 0.20$ m) in general have lower goodness-of-fit values, $R^2 = 0.85$ to 0.93, than the shallower cases. This is attributed to the deeper cases exhibiting slightly larger wake strength ($\Pi = 0.1$, where Π is Cole's wake strength) than the shallower cases ($\Pi = 0$) (see equation (5)).

For the smooth bed and compound channel cases, the power-law exponent is observed to increase systematically with flow depth and flow speed. This trend is consistent with *Chen* [1991] who observed larger values of m correspond with deeper flows. Typical examples of power-law curve fits from the smooth and rough bed cases for a range of power-law exponents are shown in Figure 3.

Due to the horizontal orientation of the ADV probe used in our experiments, measurements below $z = 0.03$ m where not possible as can be seen in Figure 3. To extrapolate the profiles to the bed, we alternatively rely on either the log law or the power law to estimate the missing data. The solid line plotted in Figure 3 corresponds to the power law, whereas the dotted line corresponds to the log-law extension to the bed. It is observed that in the near wall region, the differences are small. Systematic examination of the entire dataset revealed that the power law tends to overpredict the velocity profiles as compared with the log law in the near-wall region. The consequence of this is that integral quantities, such as the displacement thickness,

$$\delta^* = \int_0^h \left[1 - \frac{U(z)}{U_{\max}} \right] dz, \qquad (2)$$

the momentum thickness,

Figure 4. Comparison of estimations of the (a) shape factor, H and the (b) depth-averaged velocity, U_B as determined by the log law and power law. Solid line, $f(x) = x$. Magenta symbols, $h = 0.06 - 0.08$ m; blue symbols, $h = 0.10 - 0.11$ m; red symbols, $h = 0.15 - 0.16$ m; green symbols, $h = 0.20 - 0.21$ m; black symbols, $h = 0.31$ m. $\circ$, $U_B = 0.05$ m/s; $\triangledown$, $U_B = 0.09 - 0.1$ m/s; $\square$, $U_B = 0.23 - 0.24$ m/s; $\triangleright$, $U_B = 0.33 - 0.35$ m/s. Filled-in symbols indicate smooth bed cases and hollow symbols indicate rough bed cases. + symbols indicate the compound channel cases.

$$\theta^* = \int_0^h \left(\frac{U(z)}{U_{\max}} \right) \left[1 - \frac{U(z)}{U_{\max}} \right] dz, \tag{3}$$

and the shape factor, $H = \delta^*/\theta$ (depicted in Figure 4a and used in the next section) are under predicted by a small amount ($\delta_{PL}^* = 0.92(\delta_{LL}^*)$; $\theta_{PL} = 0.93(\theta_{LL})$; $H_{PL} = 0.97(H_{LL})$, where the subscripts PL and LL correspond to quantities derived from the power law and log-law extensions to the bed, respectively). From the equations given above, it can be surmised that the displacement thickness quantifies the portion of the water column that is slowed down by the bed and the momentum thickness quantifies this momentum lost to the bed. It is not surprising then that overprediction of the vertical profiles of the streamwise velocity leads to under-prediction of these quantities (which relate to the area under the velocity curve).

However, differences between the depth-averaged velocity, $U_B = 1/h \int_0^h U(z) dz$, as calculated from the power law and the log-law extensions to the bed are negligible (less than 2%) as can be seen in Figure 4b. The reason for this lack of difference can be attributed to the nature of the integral which defines the depth-averaged velocity and weights the measured ADV data in the outer layer more heavily than the extrapolated near bed data.

3.2. Development of Methodology Using In Situ Measurements
Having established that our data are well approximated by a power-law velocity distribution, we turn now to the problem of remotely predicting the velocity index and depth-averaged velocity. The crux of the problem of remotely determining the velocity index revolves entirely around remotely predicting the depth-averaged velocity, as surface measurements of velocity are readily obtainable from LSPIV techniques. We are able to remotely predict depth-averaged velocity by leveraging the technique developed in *Johnson and Cowen* [2017], which enables remote prediction of the friction velocity. Through correlation of dissipation calculated on the free surface with measured near surface values of dissipation, *Johnson and Cowen* [2017] were able to remotely predict vertical profiles of dissipation in the water column. They then inverted Nezu's universal relation for dissipation in open channel flows [see *Johnson and Cowen*, 2017, equation (6)] to solve for friction velocity. The technique enables remote prediction of the friction velocity and when coupled with surface measurements of velocity as in this work, other pertinent flow parameters can be obtained.

Numerous turbulent boundary layer and open channel flow studies [e.g., *Bandyopadhyay*, 1987; *Tachie et al.*, 2000] have noted the relationship between the shape factor, H, and the skin friction coefficient, C_f, where the shape factor, is equal to the ratio of the displacement thickness to the momentum thickness as given previously. The skin fiction coefficient is given by,

$$C_f = \frac{\tau_W}{1/2 \rho U_\infty^2},$$

(4)

where $\tau_W = u^{*2} \rho$ is the bed shear stress, which by definition is equivalent to the friction velocity (u^{*2}) squared times the fluid density (ρ) and U_∞ is the boundary layer freestream velocity, which is taken to be the surface velocity in open channel flow, $U_\infty \approx U_{surf}$ [*Nowell and Church*, 1979]. When the formula for the bed shear stress is substituted into the expression for skin friction, algebraic manipulation yields, $C_f = 2u^{*2}/(U_{surf}^2)$. Further manipulation yields, $(2/C_f)^{(1/2)} = U_{surf}/u^*$, a ratio that can be calculated remotely given the findings of *Johnson and Cowen* [2017]. Here we note the difference between this ratio and the typical ratio often used in open channel flow resistance, namely $U_{avg}/u^* = \sqrt{8/f} = C\sqrt{g} = R^{(1/6)}/(\sqrt{g}n)$ (where g is the gravitational acceleration), which can be related to the resistance formulas involving the Darcy-Weisbach friction factor, f, and Chezy's coefficient, C, and Manning's n, respectively. In assessing channel resistance typically either a depth-averaged velocity or a cross-sectional mean velocity is used. For the purpose of remotely predicting depth-averaged velocity and the velocity index, we form the ratio of the free-surface velocity with the friction velocity. In doing so, we can relate this ratio to the shape factor and predict the power-law exponent specific to each experimental case, thereby enabling remote prediction of the vertical velocity profile and depth-averaged velocity as will be outlined below.

In Figure 5 we plot the shape factor versus the ratio of the free-surface velocity with the friction velocity, both of which have been calculated or determined from the in situ ADV measurements. Following the work of *Bagherimiyab and Lemmin* [2013], we considered seven methods of estimating the friction velocity for each of our experimental cases and found that on average the variation between methods was less than 30% [*Johnson*, 2015] (consistent with the results of *Bagherimiyab and Lemmin* [2013] and *Nezu and Nakagawa* [1993]). The indirect method reported here estimates the friction velocity for each experimental case via linear extrapolation of the Reynolds stress ($-\overline{u'w'}$) plot to the bed. This estimate was refined through fitting the data to the linear distribution of the total shear stress $\tau/\rho = u^{*2}(1 - z/h)$ in a least squares sense [*Johnson and Cowen*, 2016].

We find that the ratio U_{surf}/u^* for smooth beds (Figure 5a) ranges from 16 to 23 and that this value decreases over rough beds (Figure 5b), to 13–17. We also find that the rough bed cases have slightly higher values for the shape factor, 1.51–1.66, whereas the smooth bed cases range from 1.26 to 1.37. The smooth bed values are within the expected range for turbulent boundary layers, 1.3–1.4. The overall trends are consistent with the results of *Tachie et al.* [2000] (black open circles) who report measurements conducted in an open channel for a wide range of bed roughness conditions and our expectation that flows with higher friction velocities (i.e., our rough bed cases) should have lower ratios of U_{surf}/u^*.
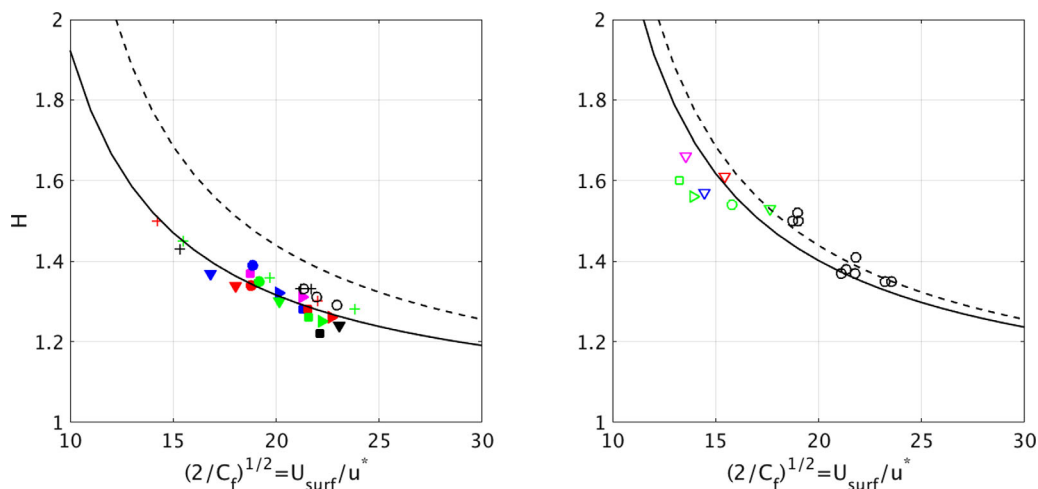

Figure 5. Shape factor versus the ratio of surface velocity to the friction velocity. (a) Smooth bed cases, smooth black line: $G = 4.8$. (b) Rough bed cases, smooth black line: $G = 5.73$. Black ∘, *Tachie et al.* [2000] smooth and rough open channel flow. Black dashed line, $G = 6.1$. See Figure 4 caption for explanation of symbols.

The present data suggest that values of the ratio of the surface velocity to the friction velocity are slightly lower for open channel flows as compared with turbulent boundary layers and this is confirmed by comparison of our results with the classic zero pressure gradient flat plate boundary layer relation given in *Tachie et al.* [2000] and plotted in Figure 5 (broken line). *Clauser* [1956] among others [e.g., *Tachie et al.*, 2000; *Bandyopadhyay*, 1987; *Ligrani*, 1989] have described the relationship between the shape factor and the skin friction coefficient with the following expression, $H = [1 - G\sqrt{(C_f/2)}]^{-1}$, where G is the Clauser shape parameter which is equal to 6.1 for zero-pressure gradient flows. The value of G that best fit our smooth bed data is $G = 4.8$ and $G = 5.73$ for our rough bed data. These are also plotted in Figures 5a and 5b, respectively (black solid line).

We attribute this difference to the fact that open channel flows typically have a smaller wake strength than boundary layer flows. When using the laws of the wall and wake to characterize boundary layer flows, the formulation is typically given as,

$$\frac{U}{u^*} = \frac{1}{\kappa} \ln\left(\frac{z u^*}{\nu}\right) + A + \frac{2\Pi}{\kappa} \sin^2\left(\frac{\pi}{2}\frac{z}{h}\right), \tag{5}$$

where κ is the von Kármán constant, A is the integration constant, and the last term on the right is the wake function where, Π is Cole's wake strength parameter. Our smooth bed cases have low wake strength, $\Pi = 0$ to 0.2 and this finding is consistent with those of *Cardoso et al.* [1989], *Nezu and Rodi* [1986], *Tachie et al.* [2000], and *Kirkgöz* [1989] who all estimate $\Pi < 0.3$. It can be deduced from equation (5) above and is beautifully illustrated in *Pope* [2000, Figure 7.28] that the wake component of the boundary layer represents the increase in velocity above that predicted by the log law (first term on the right-hand side of equation (5)), which occurs in the outer layer. Boundary layer flows typically have a wake strength of 0.55 or greater, which means these flows will have higher ratios of U/u^* in the outer layer than correspondingly similar open channel flows. We attribute the difference in the wake strength to the free-surface boundary condition.

We further observe an increase in wake strength for our rough bed cases, $\Pi = 0.2$ to 0.4. This range of values is remarkably similar to those measured by *Tachie et al.* [2000], $\Pi = 0.25$ to 0.49 for vastly different rough bed materials and relative submergence. Our rough bed consisted of a gravel bed with rms roughness height, $k_{rms} = 2.16$ cm and relative submergence, $k_{rms}/h = 0.10$ to 0.29. In the *Tachie et al.* [2000] experiments three different materials were used to comprise the rough bed (a perforated sheet with mean roughness height, $k_{mean} = 1.4$ mm, sand grains with $k_{mean} = 1.2$ mm, and wire mesh with $k_{mean} = 0.6$ mm) and the relative submergence ranged from $k_{mean}/h = 0.006$ to 0.028. Similar increases in wake strength have been observed in rough wall boundary layers studies [*Krogstad and Antonia*, 1999; *Krogstad and Antonia*, 1992; *Castro*, 2007; *Kiersbulck et al.*, 2002] and these increases have been attributed to enhanced growth rates and entrainment. The remarkable similarity in wake strength between our results and those of Tachie suggest that a singular constant for Clauser shape parameter, in the range $G = 5.7$ to 6.1, can be used to describe the relationship between U/u^* and the shape factor for rough open channel flows. In what follows we elect to use the constant $G = 5.73$ for the rough bed cases. Additional experiments are recommended to definitively determine the value of G for a range of relative submergence.

Having established that a power-law profile sufficiently describes the streamwise velocity profiles measured in this experiment, we now demonstrate that the shape factor can be related to the power-law exponent. *Hinze* [1959] derived the following relationship between the shape factor and the power-law exponent,

$$m = \frac{2}{H - 1}, \tag{6}$$

which is depicted below in Figure 6 (solid black line) along with the results determined from our in situ ADV data. Here because the shape factor is being related to the power-law exponent, we determine the shape factor using the in situ ADV data and have extrapolated the data to the bed using the power law. The resulting agreement is quite good, $R^2 = 0.97$. The slow deep cases ($H < 1.2$) here show the greatest deviation from equation (5).

From the expression given in Figure 6, the power-law exponent can be determined which permits prediction of the vertical velocity distribution. Knowledge of the power-law exponent can also be exploited to determine the velocity index coefficient. Plugging equation (1) into the definition of the depth-averaged
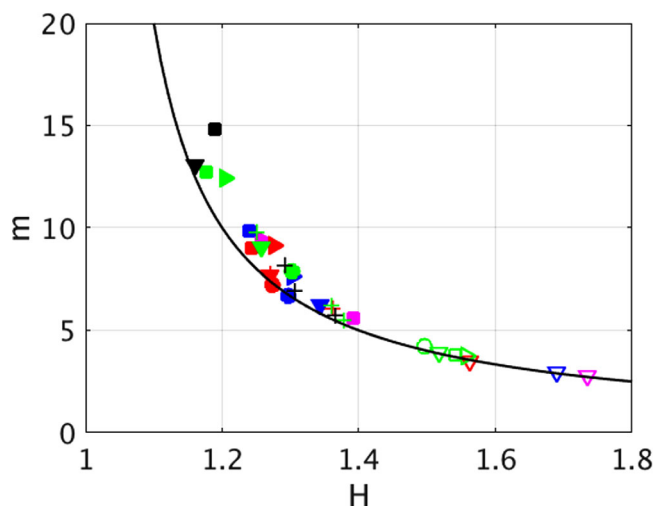
Figure 6. Power-law exponent versus shape factor. Solid line: $f(x) = 2/(H-1), R^2 = 0.97$. See Figure 4 caption for explanation of symbols.

velocity and carrying out the integration, it is a simple matter to show that $U_B/U_{surf} = m/(m+1)$. This ratio is depicted in Figure 7 where both the velocity index and power-law exponent ratio have been determined from the ADV in situ data. Here again, the agreement is quite good, $R^2 = 0.92$.

3.3. Remote Prediction of Depth-Averaged Velocity

Section 3.2 above outlines a method of remotely estimating vertical velocity profiles and the velocity index. Thus far, we have demonstrated through the use of in situ ADV data that the relations for the skin friction coefficient, the shape factor, and the power-law exponents, previously given, hold for our data set. We now combine these newly established findings with the surface velocity measurements made during the course of these experiments and with the findings of *Johnson and Cowen* [2017], which developed a methodology of remotely estimating friction velocity, to demonstrate the ability of the present proposed methodology to remotely estimate velocity index and vertical velocity profiles.

The starting point is calculating the ratio U_{surf}/u^* from the mean surface velocity profiles captured by the LSPIV system and the remotely estimated friction velocity profiles determined from *Johnson and Cowen* [2017]. Note that *Johnson and Cowen* [2017, Figures 7–9] contain plots of the bed shear stress over the channel cross section and it is a trivial matter to determine friction velocity from these profiles ($\tau_W = \rho u^{*2}$). The remotely estimated ratio U_{surf}/u^* is then sequentially converted to U_B/U_{surf} using the steps outlined in the previous section. A comparison of the free-surface estimate with in situ measurements for each step is depicted in Figure 8 below for four experimental cases.

At each step, the agreement between the estimated profiles and in situ measurements is quite good. Note that there is little variation in the velocity index for the smooth bed cases (solid red, green and blue curves) shown in Figure 8f; the exception being near the channel walls. In contrast, there is a substantial decrease in the velocity index over the rough bed (blue curve, $y/B = 0.08$ to 0.25) (the gravel bed extended over half the channel from $y/B = 0.05$ to 0.5 for the rough bed cases). Even in laboratory studies this type of variation of the velocity index is challenging and time consuming to capture with in situ sensors. The proposed remote method of estimating the velocity index, however, is able to capture this variation accurately.
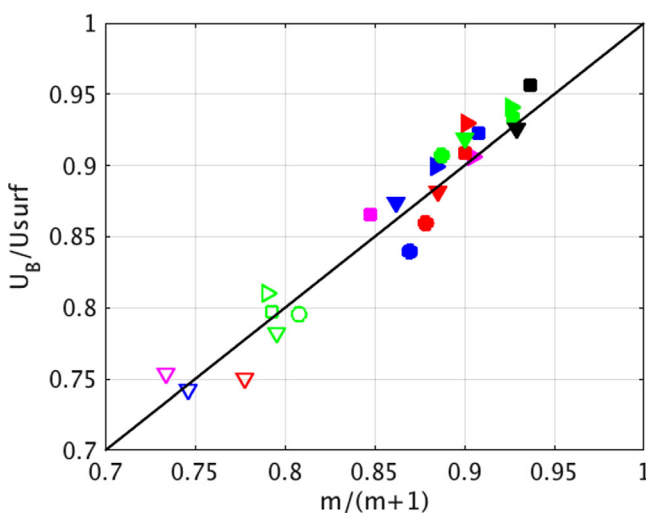
In regards to the variation of the velocity index near the channel wall, to the best of our knowledge there are only two studies which measure the velocity index close to the channel wall [*Kirkgöz and Ardichoglu*, 1997, Figure 6] and *Rantz* [1982, Figure 89] makes mention of a laboratory study but
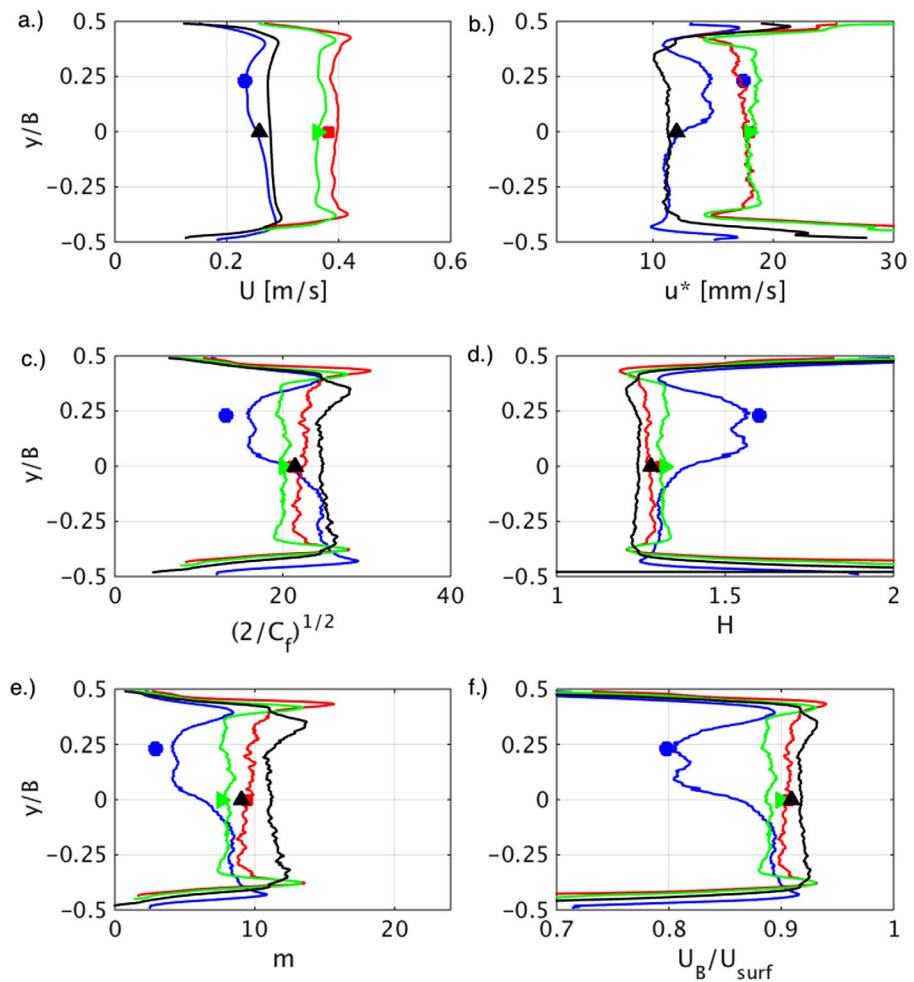

Figure 7. Velocity index versus power-law exponent ratio. Solid line: $f(x) = x, R^2 = 0.92$. See Figure 4 caption for explanation of symbols.

Figure 8. Comparison of remotely predicted profiles and in situ measurements of (a) mean surface velocity, (b) friction velocity, (c) ratio U_{surf}/u^*, (d) shape factor, (e) power-law exponent, (f) and velocity index. Blue curve is the rough bed, $h = 0.20$, $U_B = 0.18$ m/s case. Red curve is the smooth bed, $h = 0.06$, $U_B = 0.35$ m/s case. Green curve is the smooth bed, $h = 0.21$, $U_B = 0.33$ m/s case. Black curve is the smooth bed, $h = 0.15$, $U_B = 0.24$ m/s case.

provides no reference. Both studies predict an increase in the velocity index near the channel wall, similar to our results in Figure 8f above. The *Rantz* [1982] velocity index profile continues to increase as the wall is approached, however, all of our profiles of velocity index drop precipitously. Both the depth-averaged velocity and the surface velocity should tend to zero as the wall is approached, consistent with our estimation. Additional measurements close to channel walls would be helpful to clarify the behavior of the velocity index near channel walls.

Using the estimated power-law coefficient determined by the proposed technique, it is possible to compare predicted vertical velocity profiles with in situ profile measurements. Selecting the estimated power-law coefficient from the same location where the in situ measurements were made and selecting the same z measurement locations, allows for a 1:1 comparison. The results are depicted below in Figure 9 and are generally good. The largest discrepancies occur in the shallowest rough bed cases, for which it was difficult to measure accurately close to the bed (e.g. rough bed $h = 0.10$ m, $U_B = 0.05$ m/s, blue open circles).

As a final verification of the developed methodology, we recalculate volumetric discharge using the estimated profiles of the velocity index and the method outlined in *Johnson and Cowen* [2016], which used the integral length scale as a proxy for local bathymetry. We compare the recalculated volumetric discharge estimates with an independent measurement of discharge from an ultrasonic flow meter and the estimates of discharge determined in *Johnson and Cowen* [2016]. In *Johnson and Cowen* [2016] the velocity index over the field-of-view was estimated from in situ measurements. For the smooth bed cases, the value of the
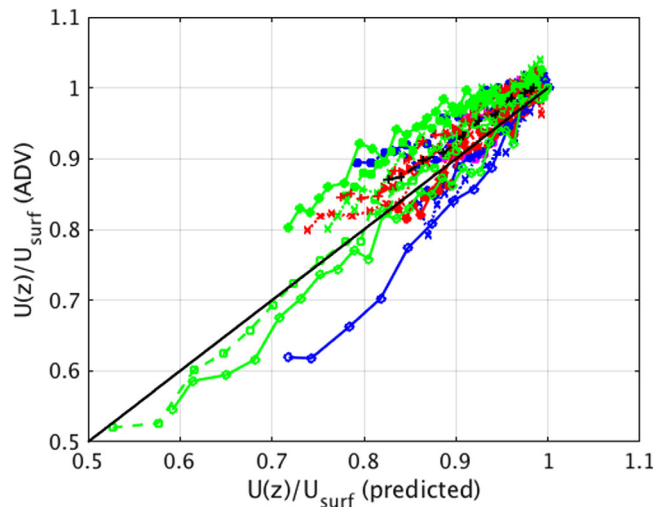
Figure 9. Predicted versus measured vertical profile of streamwise velocity. See Figure 4 caption for explanation of symbols.

velocity index measured at the channel centerline was applied to the entire surface velocity profile. For the rough bed and compound channel cases, weighted averages of the multiple in situ measurements were used.

When the methodology developed herein is applied to the data set measured in *Johnson and Cowen* [2016], improvements in the prediction of volumetric discharge are observed, albeit modest, $R^2 = 0.92$ to $R^2 = 0.93$. The comparison is depicted in Figure 10. When considered by themselves, the improvements in the prediction of discharge for the rough bed cases are greater from the methodology developed herein as compared with *Johnson and Cowen* [2016], $R^2 = 0.94$ to

$R^2 = 0.98$. We attribute this improvement to the fact that the rough bed cases exhibit a wider range of values for the velocity index owing to half the bed being composed of gravel and the other half was smooth glass. This variation is captured more accurately by the methodology developed herein as opposed to the use of weighted averages as in *Johnson and Cowen* [2016].

4. Discussion and Conclusion

Here we have developed a technique that remotely predicts vertical flow structure and the velocity index, which is typically used in conjunction with LSPIV techniques to remotely measure volumetric discharge. This technique leverages the findings of *Johnson and Cowen* [2017] and existing power-law relationships developed for turbulent boundary layer studies to predict applicable power-law exponents leading to prediction of vertical flow structure and the velocity index. The steps include:

1. Reference *Johnson and Cowen* [2016] (among others) for details on the remote estimation of the free-surface mean streamwise velocity profile.
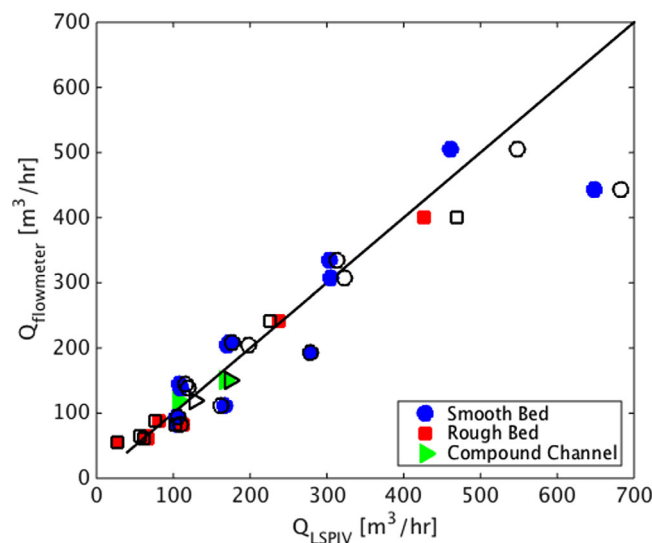

Figure 10. Improved estimates of volumetric discharge versus independent flow meter measurements. Black hollow symbols depict measurements derived following the methodology of *Johnson and Cowen* [2016].

2. Reference *Johnson and Cowen* [2017] for details on the remote estimation of $u*$.

3. Calculate the ratio $U_{surf}/u*$ from the above data.

4. Calculate the shape factor from, $H = [1 - G\sqrt{(C_f/2)}]^{-1}$. For gravel bed cases use $G = 5.73$, for smoother bed conditions use $G = 4.8$.

5. Calculate the power-law exponent using, $m = 2/(H-1)$.

6. Calculate the index velocity from the power-law coefficient $U_B/U_{surf} = m/(m+1)$.

Our outlook for a field implementation of this methodology is hopeful. We anticipate that this technique will be particularly useful for channels and rivers with strongly variable flows and

bathymetric conditions. Simple relationships that exist relating the power-law exponent to resistance coefficients and friction factors such as $m = 1.37f^{-0.43}$ *Cheng* [2007] will make this methodology useful in flow resistance studies.

Given the moderate Reynolds numbers obtained in the lab, we expect that better agreement of the data will be obtained in the field, particularly in the plot of the shape factor versus the ratio U_{surf}/u^* and for Clauser's shape parameter, G. As discussed in *Johnson and Cowen* [2016, 2017], the technique that is developed here is intended to be used at field sites that are in accord with USGS site selection guidelines (i.e., straight river reaches with approximately uniform flow, no confluences at the site, and high permanent banks [*Rantz*, 1982]).

References

Bagherimiyab, F., and U. Lemmin (2013), Shear velocity estimates in rough-bed open-channel flow, *Earth Surf. Processes Landforms*, *38*(14), 1714–1724.

Bandyopadhyay, P. R. (1987), Rough-wall turbulent boundary layers in the transition regime, *J. Fluid Mech.*, *180*, 231–266.

Bechle, A. J., C. H. Wu, W. C. Liu, and N. Kimura (2012), Development and application of an automated river-estuary discharge imaging system, *J. Hydraul. Eng.*, *138*(4), 327–339.

Blasius, H. (1913), Das ähnlichkeitsgesetz bei reibungsvorgängen in flüssigkeiten, in *Mitteilungen über Forschungsarbeiten auf dem Gebiete des Ingenieurwesens*, vol. 131, pp. 1–41, Springer, Berlin Heidelberg.

Cardoso, A. H., W. H. Graf, and G. Gust (1989), Uniform flow in a smooth open channel, *J. Hydraul. Res.*, *27*(5), 603–616.

Castro, I. P. (2007), Rough-wall boundary layers: Mean flow universality, *J. Fluid Mech.*, *585*, 469–485.

Chen, C. I. (1991), Unified theory on power laws for flow resistance, *J. Hydraul. Eng. ASCE*, *117*(3), 371–389.

Cheng, N. S. (2007), Power-law index for velocity profiles in open channel flows, *Adv. Water Resour.*, *30*(8), 1775–1784.

Clauser, F. H. (1956), The turbulent boundary layer, *Adv. Appl. Mech.*, *4*, 1–51.

Costa, J. E., K. R. Spicer, R. T. Cheng, F. P. Haeni, N. B. Melcher, E. M. Thurman, W. J. Plant, and W. C. Keller (2000), Measuring stream discharge by non-contact methods—A proof-of-concept experiment, *Geophys. Res. Lett.*, *27*(4), 553–556.

Cowen, E. A., and S. G. Monismith (1997), A hybrid digital particle tracking velocimetry technique, *Exp. Fluids*, *22*(3), 199–211.

Creutin, J. D., M. Muste, A. A. Bradley, S. C. Kim, and A. Kruger (2003), River gauging using PIV techniques: A proof of concept experiment on the Iowa River, *J. Hydrol.*, *277*(3), 182–194.

Dramais, G., J. Le Coz, B. Camenen, and A. Hauet (2011), Advantages of a mobile LSPIV method for measuring flood discharges and improving stage-discharge curves, *J. Hydro-Environ. Res.*, *5*(4), 301–312.

Efron, B., and R. J. Tibshirani (1994), *An Introduction to the Bootstrap*, vol. 57, CRC Press, Chapman & Hall/CRC, New York.

Gunawan, B., X. Sun, M. Sterling, K. Shiono, R. Tsubaki, P. Rameshwaran, and I. Fujita (2012), The application of LS-PIV to a small irregular river for inbank and overbank flows, *Flow Meas. Instrum.*, *24*, 1–12.

Harpold, A. A., S. Mostaghimi, P. P. Vlachos, K. Brannan, and T. Dillaha (2006), Stream discharge measurement using a large-scale particle image velocimetry (LSPIV) prototype, *Trans. of the ASABE*, *49*(6) 1791–1805.

Hauet, A., A. Kruger, W. F. Krajewski, A. Bradley, M. Muste, J. D. Creutin, and M. Wilson (2008), Experimental system for real-time discharge estimation using an image-based method, *J. Hydrol. Eng.*, *13*(2), 105–110.

Hinze, J. O. (1959). Turbulence: An introduction to its mechanisms and theory, Mechanical Engineering.

Honkanen, M., and H. Nobach (2005), Background extraction from double-frame PIV images, *Exp. Fluids*, *39*(3), 348–362.

Hulsing, H., W. Smith, and E. D. Cobb (1966), Velocity-head coefficients in open channels, *U.S. Geol. Surv. Water Supply Pap. 1869-C.*

Jodeau, M., A. Hauet, A. Paquier, J. Le Coz, and G. Dramais (2008), Application and evaluation of LS-PIV technique for the monitoring of river surface velocities in high flow conditions, *Flow Meas. Instrum.*, *19*(2), 117–127.

Johnson, E. (2015), The remote monitoring of surface velocity, bathymetry and discharge in rivers and open channel flows, PhD dissertation, Cornell Univ., Ithaca, New York.

Johnson, E. D., and E. A. Cowen (2016), Remote monitoring of volumetric discharge employing bathymetry determined from surface turbulence metrics, *Water Resour. Res.*, *52*, 2178–2193, doi:10.1002/2015WR017736.

Johnson, E. D., and E. A. Cowen (2017), Estimating bed shear stress from remotely measured surface turbulent dissipation fields in open channel flows, *Water Resour. Res.*, *53*, 1982–1996, doi:10.1002/2016WR018898.

Keirsbulck, L., L. Labraga, A. Mazouz, and C. Tournier (2002), Surface roughness effects on turbulent boundary layer structures, *J. Fluids Eng.*, *124*(1), 127–135.

Kim, Y., M. Muste, A. Hauet, W. F. Krajewski, A. Kruger, and A. Bradley (2008), Stream discharge using mobile large-scale particle image velocimetry: A proof of concept, *Water Resour. Res.*, *44*, W09502, doi:10.1029/2006WR005441.

Kirkgöz, M. S. (1989), Turbulent velocity profiles for smooth and rough open channel flow, *J. Hydraul. Eng.*, *115*(11), 1543–1561.

Kirkgöz, M. S., and M. Ardiçlioglu (1997), Velocity profiles of developing and developed open channel flow, *J. Hydraul. Eng.*, *123*(12), 1099–1105.

Krogstad, P. Å., and R. A. Antonia (1999), Surface roughness effects in turbulent boundary layers, *Exp. Fluids*, *27*(5), 450–460.

Krogstad, P. Å., R. A. Antonia, and L. W. B. Browne (1992), Comparison between rough- and smooth-wall turbulent boundary layers, *J. Fluid Mech.*, *245*, 599–617.

Lacey, G. (1946). A general theory of flow in alluvium, *J. Inst. Civ. Eng.*, *27*(1), 16–47.

Le Coz, J., A. Hauet, G. Pierrefeu, G. Dramais, and B. Camenen (2010), Performance of image-based velocimetry (LSPIV) applied to flash-flood discharge measurements in Mediterranean rivers, *J. Hydrol.*, *394*(1), 42–52.

Lee, H. E., C. Lee, Y. J. Kim, J. S. Kim, and W. Kim (2013), Power law exponents for vertical velocity distributions in natural rivers, *Engineering*, *5*(12), 933–942.

Ligrani, P. M. (1989), Structure of turbulent boundary layers, in *Encyclopedia of Fluid Mechanics*, pp. 121–187, Gulf Prof. Publ., Houston, Tex.

Manning, R. (1891), On the flow of water in open channels and pipes, *Trans. Inst. Civ. Eng. Ireland*, *20*, 161–207.

Manning, R. (1895), Supplement to "On the flow of water in open channels and pipes," *Trans. Inst. Civ. Eng. Ireland*, *24*, 179–207.

Mejia-Alvarez, R., and K. T. Christensen (2013), Robust suppression of background reflections in PIV images, *Meas. Sci. Tech.*, *24*(2), 027003.

Melcher, N. B., J. E. Costa, F. P. Haeni, R. T. Cheng, E. M. Thurman, M. Buursink, and K. Hayes (2002), River discharge measurements by using helicopter-mounted radar, *Geophys. Res. Lett.*, *29*(22), 41–1.

Muste, M., Z. Xiong, J. Schöne, and Z. Li (2004), Validation and extension of image velocimetry capabilities for flow diagnostics in hydraulic modeling, *J. Hydraul. Eng.*, *130*(3), 175–185.

Muste, M., I. Fujita, and A. Hauet (2008), Large-scale particle image velocimetry for measurements in riverine environments, *Water Resour. Res.*, *44*, W00D19, doi:10.1029/2008WR006950.

Muste, M., H. C. Ho, and D. Kim (2011), Considerations on direct stream flow measurements using video imagery: Outlook and research needs, *J. Hydro-environ. Res.*, *5*(4), 289–300.

Nezu, I., and H. Nakagawa (1993), *Turbulence in Open Channel Flows*, A. A. Balkema, Rotterdam, Netherlands.

Nezu, I., and W. Rodi (1986), Open-channel flow measurements with a laser Doppler anemometer, *J. Hydraul. Eng.*, *112*(5), 335–355.

Nowell, A. R., and M. Church (1979), Turbulent flow in a depth-limited boundary layer, *J. Geophys. Res.*, *84*(C8), 4816–4824.

Polatel, C. (2006), *Large-Scale Roughness Effect on Free-Surface and Bulk Flow Characteristics in Open-Channel Flows*, ProQuest., PhD diss., University of Iowa, Iowa.

Pope, S. B. (2000), *Turbulent Flows*, Cambridge Univ. Press, Cambridge, U. K.

Puleo, J. A., T. E. McKenna, K. T. Holland, and J. Calantoni (2012), Quantifying riverine surface currents from time sequences of thermal infrared imagery, *Water Resour. Res.*, *48*, W01527, doi:10.1029/2011WR010770.

Rantz, S. E. (1982), Measurement and computation of stream-flow: Measurement of stage and discharge, *U.S. Geol. Surv. Water Supply Pap.*, 2175.

Schlichting, H., K. Gersten, E. Krause, and H. Oertel (1960), *Boundary-Layer Theory*, vol. 7, McGraw-Hill, New York.

Smart, G. M., M. J. Duncan, and J. M. Walsh (2002), Relatively rough flow resistance equations, *J. Hydraul. Eng.*, *128*(6), 568–578.

Smith, W. (1969), Feasibility study of the use of the acoustic velocity meter for measurement of net outflow from the Sacramento-San Joaquin Delta in California, *U.S. Geol. Surv. Water Supply Pap. 1877*, 54 p.

Sun, X., K. Shiono, J. H. Chandler, P. Rameshwaran, R. H. J. Sellin, and I. Fujita (2010), Discharge estimation in small irregular river using LSPIV, *Proc. ICE-Water Manage.*, *163*(5), 247–254.

Tachie, M. F., D. J. Bergstrom, and R. Balachandar (2000), Rough wall turbulent boundary layers in shallow open channel flow, *J. Fluids Eng.*, *122*(3), 533–541.

Tsubaki, R., I. Fujita, and S. Tsutsumi (2011), Measurement of the flood discharge of a small-sized river using an existing digital video recording system, *J. Hydro-environ. Res.*, *5*(4), 313–321.

Willert, C. E., and M. Gharib (1991), Digital particle image velocimetry, *Exp. Fluids*, *10*(4), 181–193.

Williams, G. S., and A. Hazen (1933), *Hydraulic Tables*, 3rd ed., John Wiley, New York.